Available online at www.sciencedirect.com
ScienceDirect
Remote Sensing of Environment 108 (2007) 277–289
Remote Sensing of Environment
www.elsevier.com/locate/rse

Surface deformation of Long Valley caldera and Mono Basin, California, investigated with the SBAS-InSAR approach

P. Tizzani [a], P. Berardino [a], F. Casu [a,b], P. Euillades [c,d], M. Manzo [a,e], G.P. Ricciardi [f], G. Zeni [a,e], R. Lanari [a,*]

[a] Istituto per il Rilevamento Elettromagnetico dell'Ambiente, National Research Council, Via Diocleziano 328, I-80124 Napoli, Italy
[b] Dipartimento di Ingegneria Elettrica ed Elettronica, Università degli studi di Cagliari, Piazza d'Armi, I-09123 Cagliari, Italy
[c] Conicet, Instituto CEDIAC, Facultad de Ingenierìa, Universidad Nac de Cuyo, Mendoza, Argentina
[d] Temporarily at Istituto per il Rilevamento Elettromagnetico dell'Ambiente, National Research Council, Via Diocleziano 328, I-80124 Napoli, Italy
[e] Dipartimento di Ingegneria e Fisica dell'Ambiente, Università degli Studi della Basilicata, Viale dell'Ateneo Lucano 10, I-85100 Potenza, Italy
[f] Istituto Nazionale di Geofisica e Vulcanologia, Osservatorio Vesuviano, Via Diocleziano 328, I-80124 Napoli, Italy

Received 15 September 2006; received in revised form 13 November 2006; accepted 15 November 2006

Abstract

We investigate the surface deformation of the eastern California area that includes Long Valley caldera and Mono Basin. We apply the SAR Interferometry (InSAR) algorithm referred to as Small BAseline Subset (SBAS) approach that allows us to generate mean deformation velocity maps and displacement time series for the investigated area. The results presented in this work represent an advancement of previous InSAR studies of the area that are mostly focused on the deformation affecting the caldera. In particular, the proposed analysis is based on 21 SAR data acquired by the ERS-1/2 sensors during the 1992–2000 time interval, and demonstrates the capability of the SBAS procedure to identify and analyze displacement patterns at different spatial scales for the overall area spanning approximately 5000 km^2. Two previously unreported localized deformation effects have been detected at Paoha Island, located within the Mono Lake, and in the McGee Creek area within the Sierra Nevada mountains, a zone to the south of the Long Valley caldera. In addition a spatially extended uplift effect, which strongly affects the caldera, has been identified and analyzed in detail. The InSAR results clearly show that the displacement phenomena affecting the Long Valley caldera have a maximum in correspondence of the resurgent dome and are characterized by the sequence of three different effects: a 1992–1997 uplift background, a 1997–1998 unrest phenomenon and a 1998–2000 subsidence phase. Moreover, the analysis of the retrieved displacement time series allows us to map the extent of the zone with a temporal deformation behavior highly correlated with the detected three-phases deformation pattern: background uplift-unrest-subsidence. We show that the mapped area clearly extends outside the northern part of the caldera slopes; accordingly, we suggest that future inversion models take this new evidence into account. The final discussion is dedicated to a comparison between the retrieved InSAR measurements and a set of GPS and leveling data, confirming the validity of the results achieved through the SBAS-InSAR analysis.

Keywords: Differential SAR Interferometry; SBAS-InSAR; Microwave remote sensing; Long Valley caldera; Mono Basin; Caldera unrest

1. Introduction

The Long Valley caldera and Mono Basin are located in eastern California, in an area surrounded to the west by the Sierra Nevada and to the east by the White Mountains. The Long Valley caldera, an east–west elongate oval depression with an extent of approximately 17 km by 32 km, was formed about 0.76 Ma B.P. (Hill & Prejean, 2005). Subsequently, between 0.76 and 0.6 Ma B.P., the caldera uplift and the rhyolitic lava flows eruption, referred to as early rhyolite, formed the resurgent dome (Bailey, 1989; Hill & Prejean, 2005).

The Mono Basin consists of several landforms belonging to different volcanic centers such as the Mono and Inyo chains, the Paoha and Negit Islands and some others (see Bursik & Sieh, 1989) with the centers of the basin being formed within the last 40,000 years.

* Corresponding author. Tel.: +39 0815707999; fax: +39 0815705734.
E-mail address: lanari.r@irea.cnr.it (R. Lanari).

0034-4257/$ - see front matter © 2006 Elsevier Inc. All rights reserved.
doi:10.1016/j.rse.2006.11.015

Starting from the end of the 1970s and continuing to present, the Long Valley caldera and the Mono Basin have experienced seismicity and surface deformation above the background levels (Hill et al., 1991; Langbein et al., 1993, 1995; Langbein, 2003; Newman et al., 2006). The most recent of these phenomena affected the Long Valley caldera, characterized by a significant unrest period occurring between 1997 and 1998. In this case, an inflation phenomenon slowly started in mid-1997 and then exponentially increased in late 1997, before rapidly returning to quiescence by mid-1998. The effects of this unrest episode were recorded via the exploitation of several geophysical instruments deployed in the area (including seismometers, EDM, dilatometers, tiltmeters and GPS) and via a leveling campaign that was carried out in 1997, following those performed in 1995 and 1992 (Battaglia et al., 2003a, b, c; Langbein, 2003).

We investigate in this study the deformation of Long Valley caldera and Mono Basin by applying the differential SAR Interferometry (InSAR) technique (Gabriel et al., 1989; Massonnet et al., 1993). This approach generates spatially dense ground deformation maps, obtained by computing the phase difference (interferogram) of two temporally separated SAR images, with the measured displacements representing the projection of the surface deformation on the SAR sensor line of sight (LOS).

In particular, the InSAR results presented here have been obtained by applying the algorithm referred to as Small BAseline Subset (SBAS) approach (Berardino et al., 2002), and represent an advancement over previous InSAR studies of the area. Most of the existing literature is focused on the deformation affecting the Long Valley caldera only (Fialko et al., 2001; Hooper et al., 2004; Newman et al., 2006; Thatcher & Massonnet, 1997). In contrast, we considered an expanded investigation zone extending for approximately 5000 km^2, including Long Valley caldera and Mono Basin, and we identified and analyzed both localized and large scale deformation effects, some of these being previously unreported. Moreover, the works of Fialko et al. (2001), Newman et al. (2006) and Thatcher and Massonnet (1997) utilize a small number of interferograms spanning specific deformation episodes and generated by using conventional InSAR processing. We use a significantly larger amount of SAR data and interferograms in order to follow the evolution of the detected deformation phenomena via the generation of displacement time series relevant to the whole period of observation. In this sense, our analysis is more similar to the work of Hooper et al. (2004) that, however, is just focused on the central area of the caldera and is carried out by using a Persistent Scatterers Interferometry (PSI) technique operating on full resolution (single-look) interferograms. In contrast, the applied SBAS approach allows us to analyze averaged (multilook) interferograms, thus reducing the amount of data to be processed and being very well adapted to geophysical phenomena over large spatial scales.

The paper is organized as follows: first, the geological setting and the recent dynamics of Long Valley caldera and Mono Basin are presented. Subsequently, the SBAS algorithm is described, highlighting the key characteristics and the main

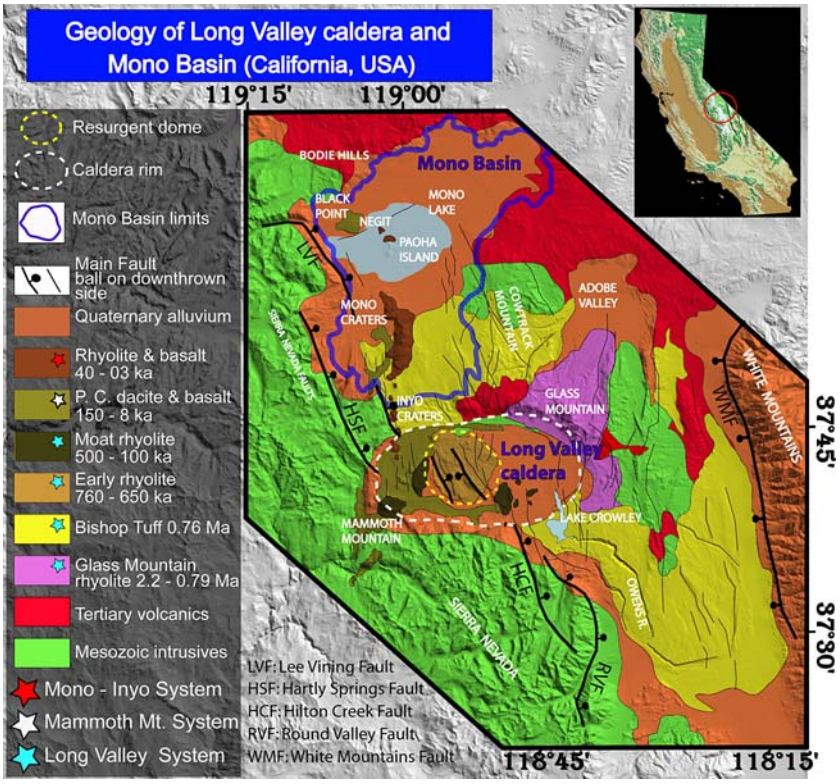

Fig. 1. Simplified geological map of Long Valley caldera and Mono Basin superimposed to the shaded relief of the Digital Elevation Model of the zone. The thick lines represent the main regional structures of the Sierra Nevada and White Mountains. The thin lines show the inner structures present in the area (data modified from Bailey (1989) and Hill and Prejean (2005)). The blue line identifies the main limits of Mono Basin as indicated by Bursik and Sieh (1989). The inset in the upper right corner shows the location of the study area.

steps of the applied procedure. This analysis is followed by the presentation and discussion of the computed SBAS-InSAR results. A comparison with independent geodetic data is then presented. The last section is focused on the main conclusions of the work and on future developments. In the Appendix, analytical details about the SBAS technique are given.

2. Geological setting and recent dynamics of Long Valley caldera and Mono Basin

The Long Valley caldera is an east–west elongate, oval depression, located northwest of the Owens Valley rift, forming an embayment in the Sierra Nevada escarpment (Bailey, 1989; Hill & Prejean, 2005), see Fig. 1. The main Long Valley caldera ring fault, presumably a sub-circular or elliptical fault (Fig. 1), is not exposed but its general location is suggested by the distribution of the moat rhyolite vents peripheral to the resurgent dome.

Volcanism in the Long Valley area (Bailey, 1989, 2004) began about 3.6 Ma B.P. with widespread eruption of trachybasaltic–trachyandesitic lavas (Hill & Prejean, 2005). At 0.76 Ma B.P., the Bishop Tuff eruption occurred forming the oval depression of the Long Valley caldera. The distribution of the resulting deposits is sketched in Fig. 1.

Recent tectonic and apparent magmatic unrest within Long Valley caldera suggest that brief episodes of such magmatic injection may have occurred between 1980 and 1986 (Bailey, 1989; Sorey et al., 2003) and in correspondence with the unrest phenomenon between 1997 and 1998 (Battaglia et al., 1999; Battaglia et al., 2003a, b; Hill et al., 2003; Langbein, 2003).

Mono Basin consists of several landforms including the Mono craters and the northern part of the Inyo chain, the Paoha and Negit Islands within the Mono Lake, Black Point, and some others (Bursik & Sieh, 1989) as sketched in Fig. 1. The centers of Mono Basin were formed within the last 40,000 years. Moreover, the spatial distribution of the different age magmas suggests that the fissure system propagated northward (Bailey, 1989; Hildreth, 2004), see Fig. 1.

The northern volcanic centers of the basin are located in Mono Lake that is a vestige of the much larger Pleistocene Lake Russell. In Mono Lake, several small dacite cinder cones and flows formed Negit Island and the northeast corner of Paoha Island about 2000 years B.P. Most of Paoha Island is composed by lake sediments that were uplifted from the lake bottom, probably by intrusion of the latter rhyolite dome (Bailey, 1989; Bursik & Sieh, 1989). The uplift of Paoha Island and extrusion of the associated rhyolite may have occurred between 1720 and 1850 A.D. (Stine, 1984).

3. Short description of the SBAS algorithm

Differential SAR interferometry is a remote sensing technique, allowing us to detect and analyze surface deformation, that was first applied to investigations of single deformation episodes (Massonnet et al., 1993; Peltzer & Rosen, 1995). More recently, it has been used to analyze the temporal evolution of deformation obtained through the inversion of an appropriate sequence of differential interferograms. Several InSAR time series approaches have been developed. One such approach, proposed by Ferretti et al. (2000) and referred to as the Permanent Scatterers (PS) technique, operates on the full resolution data. Single-look interferograms (Rosen et al., 2000) are generated with respect to a single master image without constraints on the spatial and temporal separation (baselines) of the SAR data acquisitions. Accordingly, only those pixels that are not affected by noise effects, referred to as temporal and spatial decorrelation phenomena (Zebker & Villasenor, 1992), can be exploited. Based on the PS approach, several algorithms (Hooper et al., 2004; Werner et al., 2003) have been further developed and are generally referred to as Persistent Scatterers techniques.

In this work, we apply a different approach referred to as the Small BAseline Subset algorithm (Berardino et al., 2002). This technique implements an easy combination of the SAR interferograms generated from an appropriate selection of SAR data pairs characterized by a small spatial and temporal baseline. The key objective of the data selection is to mitigate the decorrelation phenomena, maximizing the number of pixels exploited. In contrast to the Permanent and Persistent Scatterers techniques, the SBAS approach can analyze interferograms generated by a complex averaging operation, referred to as complex multilooking, applied to the full resolution data (Rosen et al., 2000). This is a relevant issue because the possibility to analyze multilook interferograms allows us to reduce the amount of data to be processed, thus simplifying the investigation of extended areas. In this section we briefly summarize the basic rationale of the SBAS technique, providing a short explanation of the main steps implementing the approach. Analytical details about the technique are given in the Appendix.

The SBAS algorithm begins with a selection of SAR image pairs, characterized by small spatial and temporal baselines, that are used to generate a set of multilook interferograms exploited by the technique. Subsequently, the coherent pixels, i.e., the pixels where the noise effects can be assumed negligible, are identified by analyzing the coherence maps that are jointly computed with the interferograms (Rosen et al., 2000). The next step is to perform phase unwrapping, i.e., the retrieval of the original (unwrapped) interferometric phase from the modulo-2π restricted (wrapped) signal directly computed from the generated interferograms. The key element of the unwrapping operation is represented by the minimum cost flow approach proposed by Costantini and Rosen (1999), that allows us to analyze data available on the sparse grid relevant to the coherent pixels (see Appendix for more details). On the unwrapped interferograms, the estimation of the deformation time series is carried out; this also includes a decoupling of the required deformation signal component from the undesired phase patterns, referred to as topographic and atmospheric artifacts. This result is obtained via the solution of a linear system of equations followed by an appropriate filtering operation based on exploiting the characteristics of these undesired phase patterns. This finally leads to the generation of the required deformation time series.

As a final remark, we underline that an estimate of the quality of the results is carried out on the pixels where the

deformation retrieval procedure has been applied. To achieve this task, we introduce the factor γ, usually referred to as temporal coherence, that is computed, pixel by pixel, as follows:

$$\gamma = \frac{\left| \sum_{k=1}^{M} \exp\left[j\left(\delta\phi_k^{\text{wrapped}} - \delta\overline{\phi}_k \right) \right] \right|}{M}, \quad 0 \le \gamma \le 1, \tag{1}$$

where M represents the number of the generated interferograms, $\delta\phi_k^{\text{wrapped}}$ and $\delta\overline{\phi}_k$, $\forall k = 1,..M$, represent the *k-th* original wrapped and the "reconstructed interferogram", respectively, the latter computed from the retrieved results. Note that for pixels where $\gamma \rightarrow 1$, we expect that no errors are present, since a nearly perfect retrieval of the original phase has been obtained. Moreover, we remark that no a priori model is assumed for the evaluation of the temporal coherence factor in Eq. (1). This is again in contrast to what is implemented in the Permanent and Persistent Scatterers techniques.

The availability of the temporal coherence factor γ in Eq. (1) leads us to identify the pixels where reliable information have been retrieved. More specifically, they are those characterized by a temporal coherence value greater than a selected threshold. Based on the selected threshold, we may identify and discard the pixels that are characterized by significant unwrapping errors and/or that "coherently" contribute only to a portion of the generated interferograms (partially coherent targets) which is not significant for retrieving reliable information.

In summary, the SBAS technique exploits standard multi-look interferograms to detect and follow the evolution of surface deformation with high degree of temporal and spatial coverage. This is achieved by using nearly all the available SAR acquisitions but exploiting only those InSAR data pairs with small baseline values.

We finally remark that the SBAS approach does not need dedicated InSAR processing and is easily implemented as a post-processing step applied to the set of interferograms that may be generated by already available interferometric data processing tools. The efficacy of the SBAS approach is highlighted in the quantitative analysis of SBAS displacement measurements by Casu et al. (2006).

Table 1
ERS SAR acquisitions on descending orbits (Track 485, Frame 2845)

Mission	Orbit	Day	Month	Year
ERS1	4638	4	6	1992
ERS1	6141	17	9	1992
ERS1	11151	2	9	1993
ERS1	12153	11	11	1993
ERS1	20513	17	6	1995
ERS1	21014	22	7	1995
ERS1	22016	30	9	1995
ERS2	2844	5	11	1995
ERS1	25523	1	6	1996
ERS2	5850	2	6	1996
ERS2	11361	22	6	1997
ERS2	13365	9	11	1997
ERS2	16872	12	7	1998
ERS2	17373	16	8	1998
ERS2	17874	20	9	1998
ERS2	18375	25	10	1998
ERS2	22383	1	8	1999
ERS2	22884	5	9	1999
ERS2	23886	14	11	1999
ERS2	27393	16	7	2000
ERS2	27894	20	8	2000

Table 2
ERS SAR interferograms computed from the acquisitions listed in Table 1

Interferogram	Bperp [m]	Btemp [days]
04 06 1992–17 09 1992	−143	105
04 06 1992–30 09 1995	−11	1213
04 06 1992–22 07 1995	183	1143
04 06 1992–05 11 1995	−96	1249
17 09 1992–05 11 1995	47	1144
17 09 1992–30 09 1995	132	1108
02 09 1993–22 06 1997	74	1389
02 09 1993–22 07 1995	−165	688
02 09 1993–11 11 1993	134	70
11 11 1993–17 06 1995	64	583
11 11 1993–22 06 1997	−60	1319
17 06 1995–16 08 1998	−4	1156
22 07 1995–30 09 1995	−194	70
22 07 1995–22 06 1997	239	701
22 07 1995–05 11 1995	−279	106
30 09 1995–05 11 1995	−85	36
05 11 1995–14 11 1999	167	1470
01 06 1996–02 06 1996	75	1
01 06 1996–09 11 1997	−98	526
01 06 1996–12 07 1998	20	771
01 06 1996–05 09 1999	−71	1191
02 06 1996–12 07 1998	−55	770
02 06 1996–09 11 1997	−174	525
22 06 1997–01 08 1999	−225	770
22 06 1997–16 08 1998	119	420
22 06 1997–09 11 1997	328	140
09 11 1997–05 09 1999	27	665
09 11 1997–12 07 1998	118	245
09 11 1997–20 09 1998	−100	315
09 11 1997–16 08 1998	−209	280
09 11 1997–16 07 2000	67	980
12 07 1998–16 07 2000	−51	735
12 07 1998–05 09 1999	−92	420
16 08 1998–20 09 1998	109	35
16 08 1998–05 09 1999	236	385
20 09 1998–16 07 2000	167	665
20 09 1998–05 09 1999	127	350
25 10 1998–01 08 1999	60	280
25 10 1998–14 11 1999	−66	385
25 10 1998–20 08 2000	4	665
01 08 1999–14 11 1999	−125	105
01 08 1999–20 08 2000	−55	385
05 09 1999–16 07 2000	40	315
14 11 1999–20 08 2000	70	280

Note that the interferogram names identify the dates of the acquisitions by using the following format: dd mm yyyy–dd mm yyyy; the factors "Bperp" and "Btemp" indicate the spatial and temporal baseline values, respectively.

4. SBAS-InSAR results

4.1. Presentation and discussion

We processed a set of 23 descending orbit SAR images (Track 485, Frame 2845), acquired by the ERS-1/2 sensors from June 1992 to October 2000, that we used to produce our

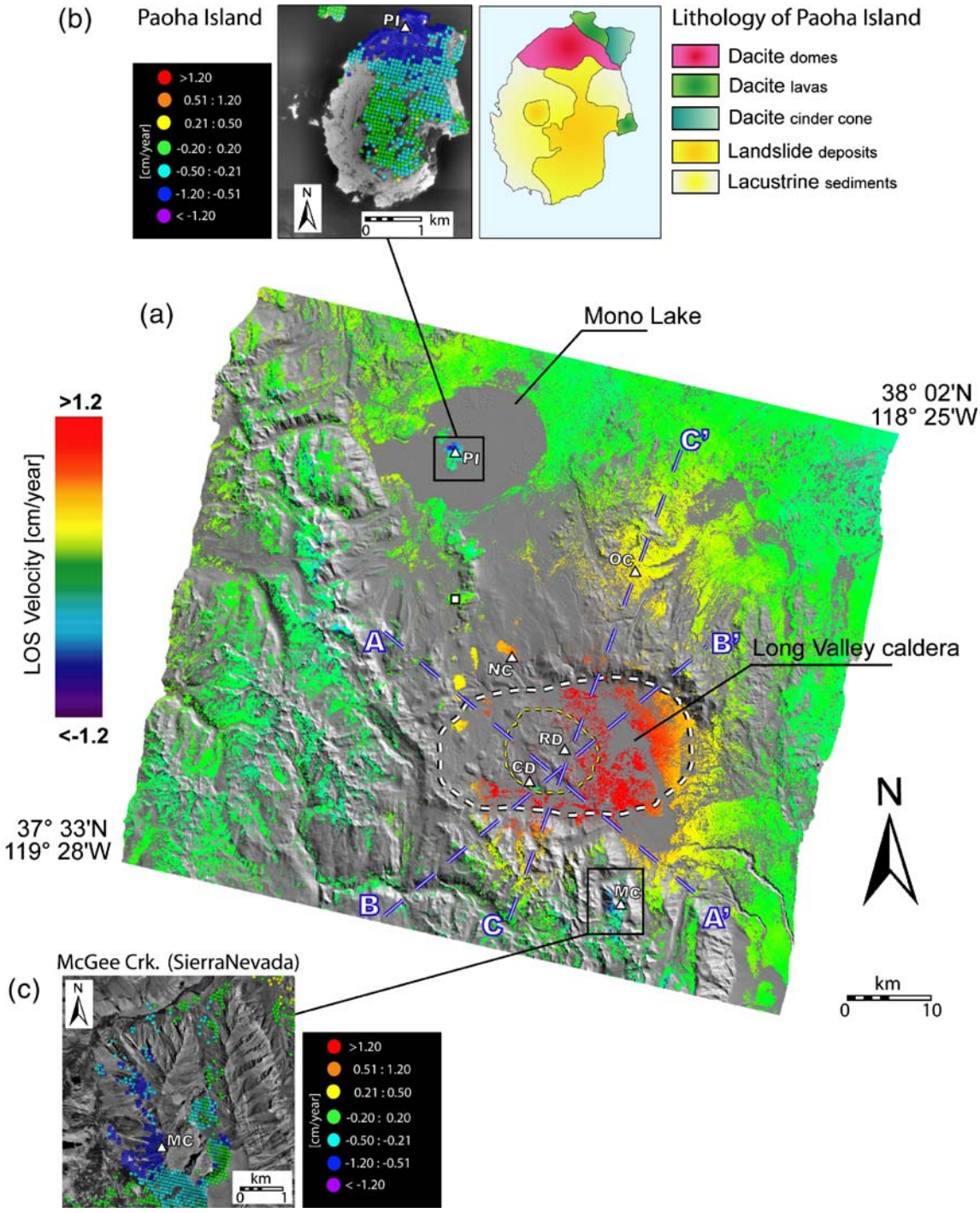

Fig. 2. SBAS-InSAR results: a) InSAR mean LOS deformation velocity map (in color) relevant to the 1992–2000 time interval, computed only in the coherent areas shown in the following Fig. 3 and superimposed to the shaded relief of the DEM (grey scale) of the investigated zone. Note that the white triangles (labeled as PI, MC, RD, NC, OC and CD) indicate the six pixels relevant to the plots shown in the following Fig. 4. The blue dashed lines indicate the three selected cross-sections relevant to the plots shown in Fig. 5 and labeled as AA′, BB′ and CC′, respectively. The boundaries of the caldera and of the resurgent dome have been identified by the dashed white and yellow lines, respectively. Finally, the white square identifies the reference SAR pixel. b) Zoomed view of Paoha Island: the InSAR mean deformation velocity map (with indicated the location of the pixel labeled as PI), superimposed to an orthophoto of the area, and the lithologic map of the island (data modified from Bailey (1989)) are shown on the left and on the right hand side of the figure, respectively. c) Zoomed view of the InSAR mean deformation velocity map relevant to the McGee Creek area superimposed to an orthophoto of the zone, with highlighted the location of the pixel labeled as MC.

interferograms. In particular, a Shuttle Radar Topography Mission (SRTM) Digital Elevation Model (DEM) (Rosen et al., 2001) of the study area and precise orbital information were used for the interferograms generation. Moreover, a complex multilook operation was performed with 4 range looks and 20 azimuth looks, resulting in a final pixel size of approximately 90 m by 90 m. Overall, we generated for each SAR acquisition the 5 interferograms with the smallest perpendicular baseline as long

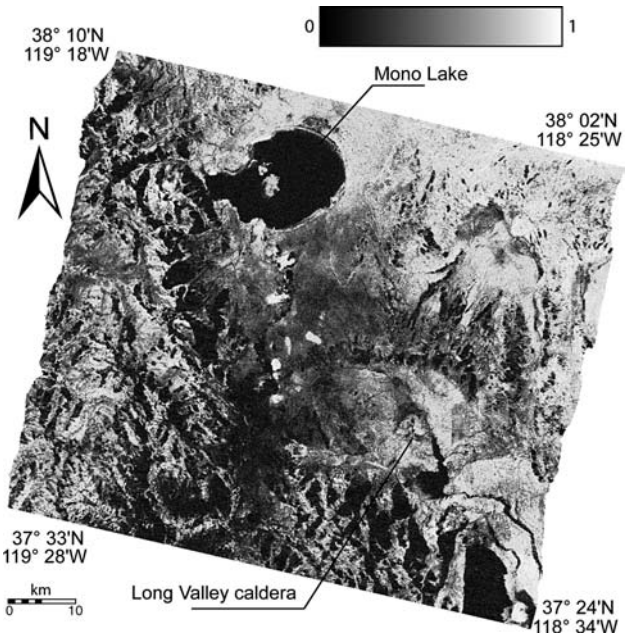

Fig. 3. Grey scale representation of the temporal coherence map relevant to the investigated area, computed according to Eq. (1).

as it is less than 350 m and the temporal separation is less than 4 years. On these interferograms a further selection was carried out; in particular, we chose those with at least 20% of the pixels characterized by a coherence value greater than 0.30. This procedure led us to exclude 24 interferograms and to remove two SAR acquisitions (November 1998 and October 2000) where the snow coverage significantly affected the interferogram's coherence, see Table 1. Accordingly, 44 interferograms were finally selected, see Table 2.

Let us now illustrate the computed SBAS-InSAR results. In order to provide an overall picture of the detected deformation pattern, we present the geocoded InSAR mean deformation velocity map superimposed on a 75 km by 75 km shaded relief of the DEM of the study area (Fig. 2a). The velocity map was computed with respect to a reference pixel represented by a white square and is relevant to coherent pixels only. Note that these pixels have been identified by using the temporal coherence map, see Fig. 3, computed according to Eq. (1); in particular, we selected those pixels characterized by a temporal coherence greater than 0.7, that is a typical value in InSAR applications (Borgia et al., 2005; Casu et al., 2006).

Several deforming areas can be identified in the mean deformation velocity map of Fig. 2a. Of particular interest are two previously unreported localized deformation effects that can be seen. One is Paoha Island located within the Mono Lake, highlighted in the left hand side of Fig. 2b. The second deformation pattern affects a zone to the south of the Long Valley caldera, in McGee Creek within the Sierra Nevada mountains; a zoomed view of this phenomenon is shown in Fig. 2c. In addition to these localized patterns, a spatially extended uplift effect is clearly visible in Fig. 2a. It strongly affects the Long Valley caldera area but additional uplifting phenomena, also in this case not reported before, are clearly visible to the north of the caldera, particularly in the area between Adobe Valley and Cowtrack Mountain (see Fig. 1 for reference). The spatial and temporal evolution of deformation for each of these deforming areas is discussed below.

Paoha Island in Mono Lake shows high temporal coherence values (thus ensuring a reliable retrieval), see Fig. 3, and is characterized by a significant subsidence of the lava domes in the northern side zone, with respect to the lacustrine and landslide sediments that form the central and southern part of

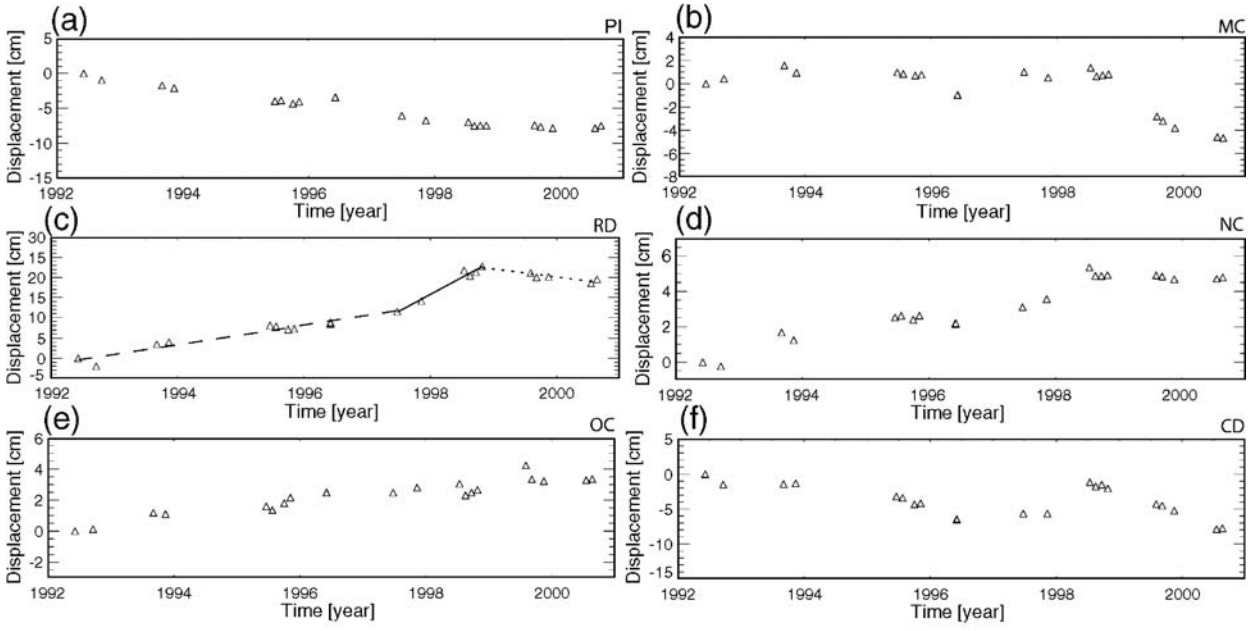

Fig. 4. InSAR LOS deformation time series for the pixels marked by the white triangles labeled in Fig. 2a as PI (Fig. 4a), MC (Fig. 4b), RD (Fig. 4c), NC (Fig. 4d), OC (Fig. 4e) and CD (Fig. 4f), respectively. Note that in Fig. 4c the best fit linear trends of the InSAR time series relevant to the 1992–1997 uplift background (dashed line), 1997–1998 unrest phenomenon (continuous line) and 1998–2000 subsidence phase (dotted line) have been plotted.

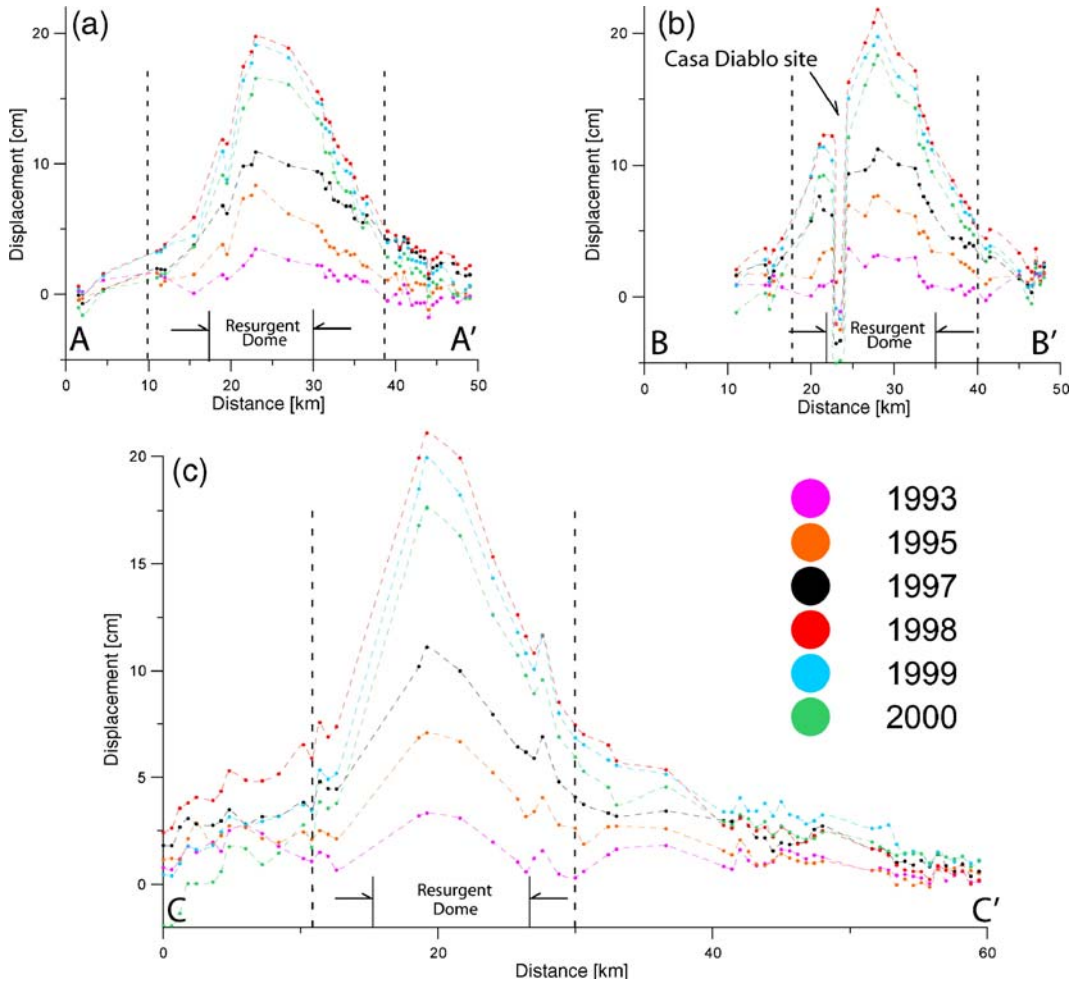

Fig. 5. Plots of the detected LOS displacements measured in correspondence of the first SAR acquisition for each year of observation (1993, 1995, 1997, 1998, 1999, 2000), and evaluated with respect to June 1992, for the three cross-sections labeled in Fig. 2a as AA′ (Fig. 5a), BB′ (Fig. 5b) and CC′ (Fig. 5c), respectively. Moreover, the beginning as well as the end of each line have been highlighted by capital letters. Note also that in Fig. 5a–c the dome and the caldera indicative boundaries have been highlighted, the latter represented by dashed vertical lines. The location of the Casa Diablo site is also highlighted in Fig. 5b. Note that the colored dots identify the data points while the dashed lines have been drawn for visualization purposes only.

the island (Fig. 2b). This could be explained as the result of an anisotropic distribution of gravitational stress due to different lithologies present in the island (lavas and landslides sediments) that load over the water-saturated floor lacustrine sediments. It is also worth noting that the deformation effect in this zone is rather continuous, as clearly shown by the plot of Fig. 4a that presents the temporal evolution of the displacements relevant to the pixel labeled as PI in Fig. 2a and b.

The McGee Creek deformation (Fig. 2c), is characterized by a nonlinear deformation behavior with a subsidence effect that is mostly concentrated in the last year of observation (see the Fig. 4b, plot of the pixel labeled as MC in Fig. 2a and c). In this case, the detected phenomenon is very likely related to a slope instability effect, although possible interaction with the dynamics of Long Valley caldera, that are discussed in the following analysis, cannot be excluded.

The large uplifting area, clearly visible in Fig. 2a, has a signal dominated by the deformation occurring in correspondence with the Long Valley caldera. In particular, to better investigate the geometry and the space-time characteristics of the deformation fields, we have identified three sections in the study area (dashed blue lines in Fig. 2a). For each of these sections, we have plotted the detected LOS deformation measured in correspondence of the first date of each year of the investigated SAR image sequence and evaluated it with respect to June 1992, which is assumed as reference[1].

In considering the Long Valley caldera and surrounding area, let us focus first on the plots shown in Fig. 4c and Fig. 5a–c. The former is relevant to the deformation time series of the pixel labeled as RD in Fig. 2a, that is located in the maximum deforming area within the resurgent dome zone. The latter are relevant to the three cross-sections labeled in Fig. 2a as AA′, BB′ and CC′, respectively, arranged with a sort of radial distribution across the resurgent dome. From the analysis of these plots it clearly appears that the deformation pattern is characterized by

[1] Note that we did not consider in our cross-sections the data relevant to 1996; in this case only two acquisitions were available to us with a very short temporal separation (1 day), not guaranteeing an effective filtering of the atmospheric phase artifacts (Casu et al., 2006).

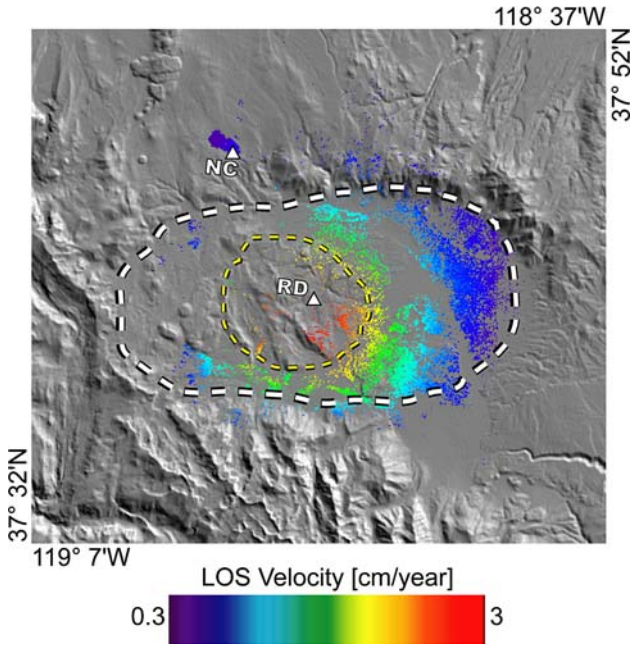

Fig. 6. Shaded relief of the DEM (grey scale) with superimposed the InSAR mean LOS deformation velocity map (in color) relevant to the area including the pixels showing a temporal deformation behavior with a correlation value greater than 0.95, with respect to the time series (see Fig. 4c) of the pixel RD located within the resurgent dome zone. Note that, at variance of Fig. 2a, no saturation of the deformation velocity values has been applied. The location of the pixel NC of Fig. 2a is also highlighted.

the sequence of three different effects: a 1992–1997 uplift background, a 1997–1998 unrest phenomenon and a 1998–2000 subsidence phase. Note that these three different effects have been highlighted in Fig. 4c where, for each time interval, the best fit linear trend of the InSAR time series has been plotted. Moreover, the location of the detected maximum displacement area, shown in Fig. 5a–c, does not change significantly passing from the background to the unrest and, finally, to the subsidence phase. This is consistent with what was previously reported by Battaglia et al. (2003a) and Langbein (2003).

We further remark that, by analyzing the retrieved deformation time series of the Long Valley caldera and surrounding area, it appears that the shape of the deformation time series inside the caldera (passing from the background to the unrest and, finally, to the subsidence phase) is also retrieved externally to the caldera rims (see for instance the plot in Fig. 4d for the pixel labeled as NC in Fig. 2a). To better clarify this issue, we have used the available InSAR results in order to detect the pixels with a temporal deformation behavior that is highly correlated (we considered the linear Pearson correlation coefficient, Stanton (2001)) with the time series of the pixel RD located within the resurgent dome zone (see Fig. 4c). The mean deformation velocity map of the pixels with a correlation value greater than 0.95 is shown in Fig. 6. It is evident that, even for a rather restrictive correlation value (0.95), there are areas located outside the northern part of the external slopes of the caldera whose deformation behavior is strongly correlated with that of the resurgent dome. We suggest that future inversion models take this behavior into account.

Note also that no spatial filtering, that may have enhanced the spatial correlation of the detected displacements, has been applied to the retrieved deformation time series. Indeed, the only spatial filtering operation that we carried out is relevant to the atmospheric artifact signals that have been detected and

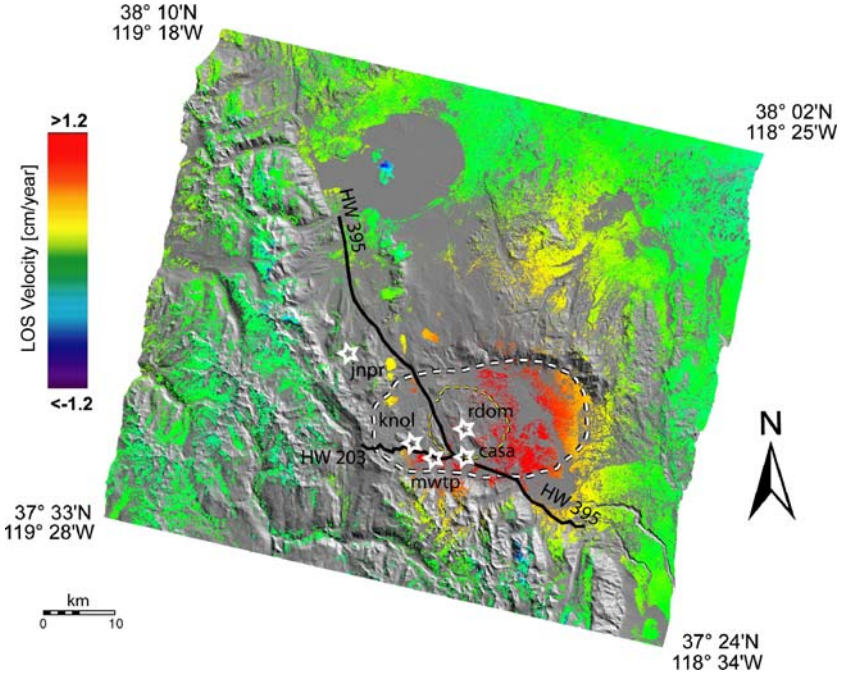

Fig. 7. InSAR mean LOS deformation velocity map shown in Fig 2a, with superimposed the white stars marking the GPS stations belonging to the USGS surveillance network where a time-overlap with the SAR measurement is available. The black lines labeled as HW 395 and HW 203 indicate two leveling paths present in the area. Also in this case the boundaries of the caldera and of the resurgent dome have been identified by the dashed white and yellow lines, respectively.

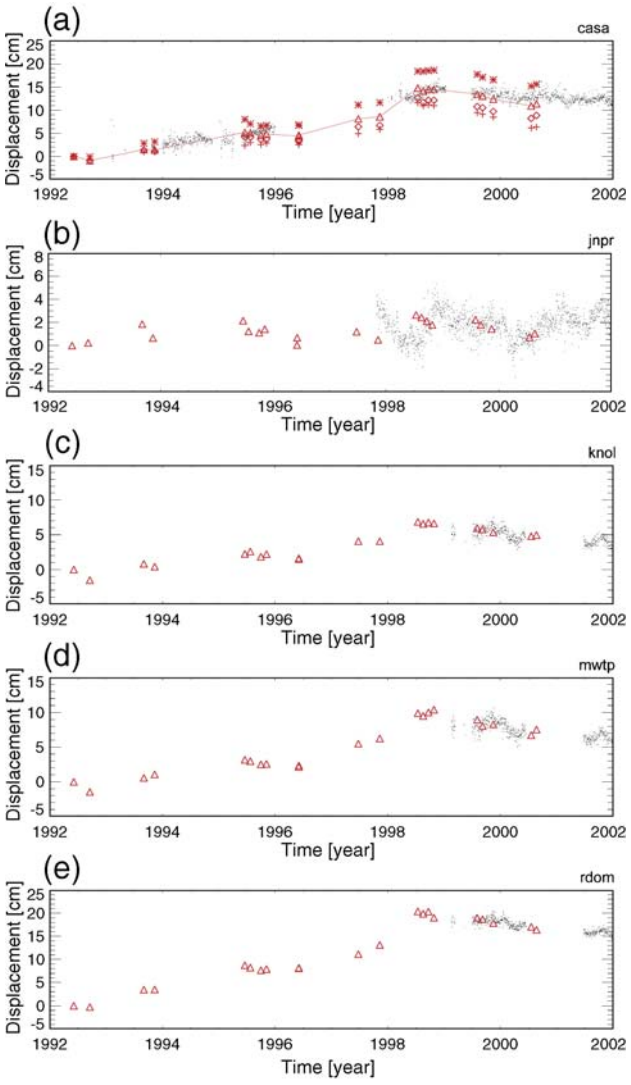

Fig. 8. Comparison between the InSAR LOS deformation time series (red triangles) and the corresponding GPS measurements projected on the SAR sensor LOS (black dots), for the pixels marked by the white stars in Fig. 7, labeled as "casa" (Fig. 8a), "jnpr" (Fig. 8b), "knol" (Fig. 8c), "mwtp" (Fig. 8d) and "rdom" (Fig. 8e), respectively. Note that, in the plot relevant to the "casa" site (Fig. 8a) we present the InSAR time series relevant to three SAR pixels (red asterisks, diamonds and crosses) surrounding the GPS station. Moreover, the time series obtained by averaging the data of these three pixels is also represented by using the red triangle symbols.

subsequently filtered out; accordingly, this filtering step cannot have affected the spatial correlation of the retrieved displacement time series.

We further remark that additional analysis will also deserve the previously unreported uplifting phenomena that occurs to the north of the caldera, particularly in the area between Adobe Valley and Cowtrack Mountain, where a rather continuous deformation trend has been detected with a maximum value of the mean deformation velocity of about 0.4 cm/year. This corresponds to the pixel identified by the white triangle labeled as OC in Fig. 2a, whose deformation time series is shown in Fig. 4e. We may reasonably say that this area and, more generally, those external to the map of Fig. 6 but showing a significantly uplift effect, are still affected by the dynamics associated with the stress source of the Long Valley caldera.

Finally, we note the temporal evolution of deformation in the Casa Diablo geothermal area within the Long Valley caldera (Fig. 4f, corresponding to the pixel labeled as CD in Fig. 2a). In this case, it clearly appears that the general subsidence trend, due to the geothermal station activity, is interrupted by the caldera uplift during the unrest episode, see also the cross-section BB′ presented in Fig. 5b. This effect is already known (Howle et al., 2003) but it is reported here to underline the retrieval capability of the SBAS approach of such localized effects even if they occur in areas with a significantly different deformation behavior.

4.2. Comparison with GPS and leveling data

We confirmed the validity of the results achieved via the SBAS approach by carrying out a comparison between the InSAR and a GPS and leveling network in the investigated area (Fig. 7). In particular, we have exploited the data collected by the USGS continuous GPS surveillance network (USGS), which now includes 17 GPS stations operating since early 1993. We selected those stations where a time-overlap with the SAR measurements is available. These stations are identified in Fig. 7 by white stars and are labeled as "casa", "jnpr", "knol", "mwtp" and "rdom". For each one of the selected GPS stations, we compared the homologous InSAR and GPS time series, the latter filtered by the regional trend and projected on the SAR sensor line of sight in order to be consistent with the radar observations.

The results of this comparison, presented in the plots of Fig. 8, show good agreement between the InSAR (red triangles) and GPS (black dots) measurements. For the "casa" station site (Fig. 8a), due to the lack of a coherent pixel in correspondence of the GPS site, we have performed the comparison by averaging the InSAR measurements of three pixels surrounding the GPS station. These averaged data are represented in the plot by the red

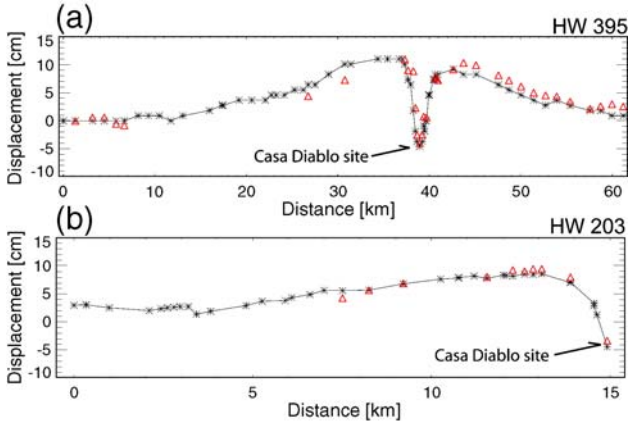

Fig. 9. Comparison between the cumulative displacements computed in the 1992–1997 time interval from the InSAR (red triangles) and the leveling (black asterisks) data, the latter projected in LOS, for the two leveling lines labeled in Fig. 7 as HW 395 (Fig. 9a) and HW 203 (Fig. 9b), respectively. The location of the Casa Diablo site is also highlighted.

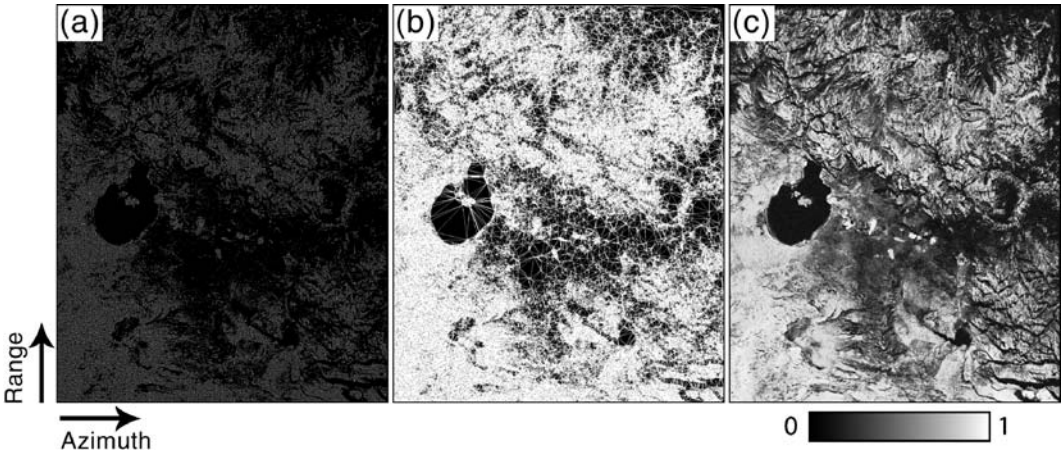

Fig. 10. InSAR products relevant to the SAR data analyzed in Section 4, represented in the sensor geometry: a) coherence mask (coherent pixels are in white); b) Delaunay triangulation of the coherence mask presented in a); c) temporal coherence map (grey scale).

triangles while the original InSAR measurements relevant to the three selected pixels are indicated by the red asterisks, diamonds and crosses, respectively. The generally good agreement between the InSAR and the LOS-projected GPS data is evident also in this case. We provided additional quantitative information by computing the standard deviation of the differences between the InSAR and the LOS-projected GPS measurements shown in Fig. 8, where available; the resulting standard deviation is about 1.3 cm. Note that this value is greater than the 5.6 mm computed by Casu et al. (2006) by comparing InSAR deformation time series with GPS measurements available through the SCIGN network of the Los Angeles area (Southern California). We interpret this difference as due to the rather small temporal overlap between the two data set and, particularly, to the significantly more limited amount of SAR data available in this study; indeed, we used 21 images for the InSAR time series generation vs. the 42 ones exploited by Casu et al. (2006). This represents a limiting factor for what concerns the atmospheric filtering operation, justifying the increase of the standard deviation value.

In the present study, we also considered the leveling data acquired from the USGS network present in the region, consisting of approximately 350 benchmarks monitored through survey campaigns. We identified (Fig. 7) two paths, following the Highways 395 and 203, respectively, for which the data for 103 benchmarks were available to us (Battaglia et al., 2003c). For each leveling line, we plotted (Fig. 9) the cumulative displacements for 1992–1997 evaluated from the InSAR (red triangles) and the leveling (black asterisks) data. The former was computed for coherent pixels only and the latter projected in the radar LOS. In contrast to the SAR/GPS comparison (where no assumptions were carried out on the displacement characteristics), we have assumed in this case that the detected deformation was vertical, since the leveling measurements can only reveal the vertical component of the displacements. The above assumption is very likely responsible for some differences between the SAR and leveling data, which appear in the right hand side portion of the plots of Fig. 9; note that in these areas significant horizontal deformation are present, as discussed by Battaglia et al. (2003a) and Langbein (2003). In any case, a rather good agreement between the deformation profiles available from the leveling data and from the InSAR measurements is observed.

Similarly to what was done for GPS data, we have computed for the coherent pixels the standard deviation of the differences between the InSAR and the LOS-projected leveling measurements shown in Fig. 9: we obtained a standard deviation value of approximately 1.5 cm. Also in this case the result is greater than the 4.3 mm reported in Casu et al. (2006) and again this disagreement can be partially attributed to the more limited amount of available SAR data; moreover, the previously reported horizontal deformation components, that are present in the area, also play a significant role.

5. Conclusions and future developments

This paper is focused on the investigation of the surface deformation affecting an area of approximately 5000 km^2 that includes Long Valley caldera and Mono Basin, California. The overall analysis is based on the exploitation of the SBAS-InSAR approach applied to a SAR data set acquired by the ERS-1 and ERS-2 sensors during the 1992–2000 time interval.

This study demonstrates the capability of the SBAS procedure to investigate the space-time characteristics of the deformation affecting the overall area and its capability to generate detailed InSAR derived products. Moreover, this analysis clarifies the relevance that the joint exploitation of the spatial and temporal information relevant to the retrieved displacements may have for discriminating spatially extended effects from local deformation patterns. In particular, two previously unreported localized deformation have been detected. The first is at Paoha Island located within the Mono Lake. The second affects a zone to the south of the Long Valley caldera, in McGee Creek within the Sierra Nevada mountains. In addition to these localized patterns, a spatially extended uplift effect has been identified. It strongly affects the Long Valley caldera area but additional uplifting phenomena, also in this case

not reported before, are clearly visible to the north of the caldera particularly in the area between Adobe Valley and Cowtrack Mountain. Also, it has been shown that the displacement phenomena at Long Valley have a maximum in correspondence to the resurgent dome and are characterized by the sequence of three different effects: a 1992–1997 uplift background, a 1997–1998 unrest phenomenon and a 1998–2000 subsidence phase. Moreover, we have identified the area where temporal deformation behavior is highly correlated with that of the resurgent dome. We remark that this zone also extends outside the northern part of the external slopes of the caldera.

Finally, a comparison between the InSAR measurements and a set of geodetic data has been presented, confirming the validity of the results achieved through the SBAS-InSAR analysis. In particular, we have shown that the computed standard deviation values of the differences between the InSAR and the LOS-projected GPS and leveling measurements are of about 1.3 cm and 1.5 cm, respectively.

As an additional remark, we also want to stress that this kind of InSAR study is nowadays not only feasible, as shown in this work, but that the produced results may be easily made accessible to the scientific community. The deformation measurements from this study can be analyzed via the web by connecting at the IREA-CNR InSAR WEB GIS page (IREA). Through this system, it is possible to query the data set relevant to the Long Valley caldera and Mono Lake zones, getting information on the spatial and temporal characteristics of the detected displacements. Indeed, it is possible to zoom in an area of interest and also to query, for each coherent pixel, the retrieved deformation time series.

The availability of just one LOS-projected displacement component did not allow us to carry out an investigation of the horizontal and vertical components of the detected deformation. The decoupling of the east–west and vertical deformation components can be achieved by using SAR data acquired from both ascending and descending orbits, as shown in previous studies by Borgia et al. (2005), Lundgren et al. (2004) and Manzo et al. (2006). However, this was not possible in this study because the availability of ascending data collected by the ERS systems is very limited for the investigated area. The exploitation of data acquired by the ENVISAT-ASAR sensor (Desnos et al., 1999), characterized by a significant multi-angle viewing capability, is foreseen in future analyses.

Acknowledgments

This work has been sponsored by the (Italian) National Group for Volcanology (GNV) of the National Institute of Geophysics and Volcanology (INGV), under the contract "GNV — Campi Flegrei" that is focused on a comparative analysis between the Long Valley (California) and Campi Flegrei (Italy) calderas. This study is also supported by the European Community on Provision 3.16, under the project of the Regional Center of Competence Analysis and Monitoring of the Environmental Risk (CRdC-AMRA). We thank the European Space Agency (ESA), which provided the ERS SAR data relevant to the Long Valley caldera, that we obtained through WInSAR in collaboration with Dr. Paul Lundgren (JPL, Caltech) and Dr. Andrew Hooper (Stanford University). The GPS and the leveling measurements were obtained through the USGS (http://pubs.usgs.gov/dds/dds-81). Moreover, the DEM of the investigated zone was acquired through the SRTM archive and precise ERS-1/2 satellite orbit state vectors were provided by the Technical University of Delft, The Netherlands. The orthophotos of Long Valley are courtesy of USGS.

We thank Dr. Paul Lundgren and Dr. Falk Amelung for their contribution to the revision process of the manuscript. Thanks are also due to Prof. Sean Buckley for correcting the manuscript and to Dr. Charles Werner and Dr. Andrew Hooper for their helpful comments.

Appendix

In this section, we provide some analytical details about the SBAS approach. We will follow the same notation as Berardino et al. (2002) and we will assume the availability of a set of $N+1$ SAR images relative to the same area, acquired at the ordered times $(t_0,\ldots,t_N)$ and co-registered with respect to a single image (referred to as master) in order to have a common reference grid.

The first step of the SBAS technique is the generation of a number, say M, of multilook differential interferograms, each of these representing the phase difference between SAR image pairs after removal of the topographic phase contribution (Massonnet et al., 1993). A key issue of the SBAS procedure is the appropriate selection of the data pairs used to generate the interferograms, whose main objective is to mitigate the decorrelation phenomena that decrease the signal-to-noise ratio of the interferometric phase (Zebker & Villasenor, 1992). The above mentioned SAR image pairs selection is based on the introduction of constraints on the maximum spatial and temporal baselines. Moreover, an additional selection is carried out on the generated interferograms in order to choose those with a significant amount of coherent pixels, the latter identified from the spatial coherence maps jointly computed with the interferograms. Subsequently, we generate the so-called "coherence mask" (Fig. 10a) obtained by considering those pixels that, for a significant portion or even for the entire interferogram sequence, have an estimated spatial coherence value greater than a selected threshold (typically 0.3).

The next step implements the phase unwrapping of the wrapped phase signal computed from the selected interferograms. This operation is carried out by applying the minimum cost flow (MCF) phase unwrapping algorithm proposed by Costantini and Rosen (1999), that allows us to process data available on the sparse grid relevant to the previously generated coherence mask. To achieve this task, we first apply the Delaunay triangulation (Delaunay, 1934) to the available coherence mask, see Fig. 10b; this step allows us to define, as neighboring points, those that are the extremes of each triangle edge and, as elementary cycles, the triangles themselves. For each interferogram the unwrapping operation involves two basic steps: first of all, we compute an initial estimate of the unwrapped phase difference between neighboring pixel pairs, from the wrapped interferogram. Subsequently, we determine a

(discrete) irrotational field whose components are close to the initial estimates generated in the previous step. The final integration of the determined irrotational vector field leads to the generation of the unwrapped phase but for an additive constant.

At this stage, the unwrapped interferograms are interpolated and calibrated with respect to a single pixel (often referred to as reference SAR pixel) located in an area that can be assumed stable or, at least, with a known deformation behavior. Note also that, in contrast to the Permanent and Persistent Scatterers techniques (Ferretti et al., 2000; Hooper et al., 2004; Werner et al., 2003), no hypothesis is done, for what concerns the implemented MCF phase unwrapping procedure, on the temporal behavior (for instance, linear deformation) of the InSAR phase signal variation between adjacent coherent pixels.

Let us now refer to a generic pixel of azimuth and range coordinates (x,r). The expression of the generic *k-th* unwrapped interferogram computed from the SAR acquisitions at times t_B and t_A, according to Berardino et al. (2002), is the following:

$$\begin{aligned}\delta\phi_k(x,r) = \phi(t_B,x,r) - \phi(t_A,x,r) \approx \frac{4\pi}{\lambda}\left[d(t_B,x,r) - d(t_A,x,r)\right] \\ + \Delta\phi_k^{\text{topo}}(x,r) + \Delta\phi_k^{\text{atm}}(t_B,t_A,x,r) \\ + \Delta n_k(x,r)\end{aligned} \tag{2}$$

with

$$\Delta\phi_k^{\text{topo}}(x,r) \approx \frac{4\pi}{\lambda}\frac{B_{\perp_k}\Delta z(x,r)}{r\sin\vartheta} \tag{3}$$

wherein $k \in (1,..,M)$, λ is the transmitted signal central wavelength, $\phi(t_B,x,r)$ and $\phi(t_A,x,r)$ represent the phases of the two images involved in the interferogram generation. For the right hand side of the last identity in Eq. (2), $d(t_B,x,r)$ and $d(t_A,x,r)$ are the LOS projections of the cumulative deformation at times t_B and t_A, with respect to the instant t_0 assumed as a reference and implying $\phi(t_0,x,r)=0$, $\forall(x,r)$. The second term $\Delta\phi_k^{\text{topo}}(x,r)$, whose expression is reported in Eq. (3), accounts for possible topographic artifacts $\Delta z(x,r)$ that can be present in the Digital Elevation Model used for removing the topographic phase contribution within the interferogram generation process. The term $\Delta\phi_k^{\text{atm}}(t_B,t_A,x,r)$ accomplishes for possible atmospheric inhomogeneities between the two acquisitions (Goldstein, 1995), and the last factor $\Delta n_k(x,r)$ accounts for the noise effects. Finally, in Eq. (3), the factor $B_{\perp_k}$ represents the perpendicular baseline component and ϑ the SAR sensor look angle.

The Eqs. (2) and (3) allow us to define a system of equations in the $N+1$ unknowns $[\phi(t_1,x,r),..,\phi(t_N,x,r),\Delta z(x,r)]$, whose solution is carried out by applying the Singular Value Decomposition (SVD) method for each coherent pixel. Note that again no a priori knowledge about the temporal behavior of the investigated deformation is assumed within the inversion process.

At this stage, we may compute the temporal coherence map, based on Eq. (1), in order to get an estimate of the quality of the obtained results. Moreover, in order to spatially "expand" the successfully retrieved data, a region growing operation, following the lines of the work of Xu and Cumming (1999), is implemented. The final temporal coherence map is obtained after this operation, see Fig. 10c.

We further remark that, after resolving the system of Eqs. (2) and (3), an evaluation and removal of the atmospheric phase artifacts $\Delta\phi_k^{\text{atm}}(t_B,t_A,x,r)$, see Eq. (2), is needed in order to provide an estimate of the line of sight deformation signal $d(t_i,x,r)$, $\forall i=0,..,N$. Accordingly, the final step of the SBAS algorithm is focused on detecting possible atmospheric artifacts. This operation, rather similar to what is carried out by the Permanent Scatterers procedure, is based on the observation that the atmospheric phase signal component is highly correlated in space but poorly in time (see Ferretti et al. (2000) and Goldstein (1995)). Accordingly, the undesired atmospheric phase signal is estimated from the time series computed by solving the system of equations based on Eqs. (2) and (3), $\forall k \in (1,..,M)$, through the cascade of a lowpass filtering step in the two-dimensional spatial domain followed by a temporal highpass filtering. The spatial filtering is implemented by using a box filter with spatial extent of approximately 1 km in azimuth and range, consistent with the spatial correlation length of the atmospheric phase signal (Hanssen, 2001). This step is followed by a temporal highpass filtering operation performed with respect to the time variable via a triangular window whose temporal extension is typically of 300 days. Following their identification, the atmospheric artifacts are removed and the generation of the final deformation time series is computed.

References

Bailey, R. A. (1989). Geologic map of Long Valley caldera, Mono-Inyo craters volcanic chain, and vicinity, Eastern California, to accompany map I-1993. Department of Interior USGS.

Bailey, R. A. (2004). Eruptive history and chemical evolution of the precaldera and postcaldera basalt-dacite sequences, Long Valley, California: Implications for magma sources, current magmatic unrest, and future volcanism. *United States Geological Survey Professional Paper* (pp. 1692).

Battaglia, M., Roberts, C., & Segall, P. (1999, September 24). Magma intrusion beneath Long Valley caldera confirmed by temporal changes in gravity. *Science*, *285*.

Battaglia, M., Segall, P., Murray, J., Cervelli, P., & Langbein, J. (2003a). The mechanics of unrest at Long Valley caldera, California: 1. Modeling the geometry of the source using GPS, leveling and two-color EDM data. *Journal of Volcanology and Geothermal Research*, *127*(3–4), 195–217.

Battaglia, M., Segall, P., & Roberts, C. (2003b). The mechanics of unrest at Long Valley caldera, California. 2. Constraining the nature of the source using geodetic and micro-gravity data. *Journal of Volcanology and Geothermal Research*, *127*(3–4), 219–245.

Battaglia, M., Williams, M. J., Venezky, D. Y., Hill, D. P., Langbein, J. O., Farrar, C. D., Howle, J. F., Sneed, M., & Segall, P. (2003). *The Long Valley Caldera GIS Database.* Available online at http://pubs.usgs.gov/dds/dds-81/

Berardino, P., Fornaro, G., Lanari, R., & Sansosti, E. (2002). A new algorithm for surface deformation monitoring based on Small Baseline Differential SAR Interferograms. *IEEE Transactions on Geoscience and Remote Sensing*, *40*(11), 2375–2383.

Borgia, A., Tizzani, P., Solaro, G., Manzo, M., Casu, F., Luongo, G., Pepe, A., Berardino, P., Fornaro, G., Sansosti, E., Ricciardi, G. P., Fusi, N., Di Donna, G., & Lanari, R. (2005). Volcanic spreading of Vesuvius, a new paradigm for interpreting its volcanic activity. *Geophysical Research Letters*, *32*, L03303. doi:10.1029/2004GL022155

Bursik, M., & Sieh, K. (1989). Range-front faulting and volcanism in the Mono Basin, Eastern California. *Journal of Geophysical Research*, *94*, 15587–15609.

Casu, F., Manzo, M., & Lanari, R. (2006). A quantitative assessment of the SBAS algorithm performance for surface deformation retrieval from DInSAR data. *Remote Sensing of Environment*, *102*, 195−210. doi:10.1016/j.rse.2006.01.023

Costantini, M., & Rosen, P. A. (1999). A generalized phase unwrapping approach for sparse data. *IGARSS'99 Proceedings, June 1999, Hamburg, Germany* (pp. 267−269).

Delaunay, B. (1934). Sur la sphere vide. *Bulletin of Academy of Sciences of the USSR* (pp. 793−800).

Desnos, Y. L., Laur, H., Lim, P., Meisl, P., & Gach, T. (1999). The ENVISAT-1 advanced synthetic aperture radar processor and data products. *IGARSS'99 Proceedings, June 1999, Hamburg, Germany* (pp. 1683−1685).

Ferretti, A., Prati, C., & Rocca, F. (2000). Non-linear subsidence rate estimation using Permanent Scatterers in Differential SAR Interferometry. *IEEE Transaction on Geoscience and Remote Sensing*, *38*(5), 2202−2212.

Fialko, Y., Simons, M., & Khazan, Y. (2001). Finite source modelling of magmatic unrest in Socorro, New Mexico, and Long Valley, California. *Geophysical Journal International*, *146*(1), 191−200.

Gabriel, A. K., Goldstein, R. M., & Zebker, H. A. (1989). Mapping small elevation changes over large areas: Differential interferometry. *Journal of Geophysical Research*, *94*, 9183−9191.

Goldstein, R. M. (1995). Atmospheric limitations to repeat-track radar interferometry. *Geophysical Research Letter*, *22*, 2517−2520.

Hanssen, R. (2001). *Radar Interferometry. Kluwer Academic Publishers.*

Hildreth, W. (2004). Volcanological perspectives on Long Valley, Mammoth Mountain, and Mono Craters: Several contiguous but discrete systems. *Journal of Volcanology and Geothermal Research*, *136*, 169−198.

Hill, D. P., Johnston, M. J. S., Langbein, J. O., McNutt, S. R., Miller, C. D., Mortensen, C. E., Pitt, A., & Rojstaczer, S. (1991). Response plans for volcanic hazards in the Long Valley caldera and Mono Craters area, California. *U.S. Geological Survey Open-File Report* (pp. 91−270). U.S. Government Printing Office.

Hill, D. P., Langbein, J. O., & Prejean, S. (2003). Relations between seismicity and deformation during unrest in Long Valley Caldera, California, from 1995 through 1999. *Journal of Volcanology and Geothermal Research*, *127*(3–4), 175−193.

Hill, D. P., & Prejean, S. (2005). Magmatic unrest beneath Mammoth Mountain, California. *Journal of Volcanology and Geothermal Research*, *146*(4), 257−283.

Hooper, A., Zebker, H., Segall, P., & Kampes, B. (2004). A new method for measuring deformation on volcanoes and other natural terrains using InSAR persistent scatterers. *Geophysical Research Letters*, *31*, L23611. doi:10.1029/2004GL0217372

Howle, J. F., Langbein, J. O., Farrar, C. D., & Wilkinson, S. K. (2003). Deformation near the Casa Diablo geothermal well field and related processes Long Valley caldera, Eastern California, 1993–2000. *Journal of Volcanology and Geothermal Research*, *127*(3–4), 365−390.

IREA, http://www.irea.cnr.it/webgis/terra.html

Langbein, J. O. (2003). Deformation of the Long Valley Caldera, California: inferences from measurements from 1988 to 2001. *Journal of Volcanology and Geothermal Research*, *127*(3–4), 247−267.

Langbein, J. O., Dzurisin, D., Marshall, G., Stein, R., & Rundle, J. (1995). Shallow and peripheral volcanic sources of inflation revealed by modeling two-color geodimeter and leveling data from Long Valley caldera, California, 1988−1992. *Journal of Geophysical Research*, *100*, 12487−12495.

Langbein, J. O., Hill, D. P., Parker, T. N., & Wilkinson, S. K. (1993). An episode of re-inflation of the Long Valley caldera, eastern California, 1989–1991. *Journal of Geophysical Research*, *98*, 15851−15870.

Lundgren, P., Casu, F., Manzo, M., Pepe, A., Berardino, P., Sansosti, E., & Lanari, R. (2004). Gravity and magma induced spreading of Mount Etna volcano revealed by satellite radar interferometry. *Geophysical Research Letters*, *31*, L04602. doi:10.1029/2003GL018736

Manzo, M., Ricciardi, G. P., Casu, F., Ventura, G., Zeni, G., Borgström, S., Berardino, P., Del Gaudio, C., & Lanari, R. (2006). Surface deformation analysis in the Ischia Island (Italy) based on spaceborne radar interferometry. *Journal of Volcanology and Geothermal Research*, *151*, 399−416.

Massonnet, D., Rossi, M., Carmona, C., Adragna, F., Peltzer, G., Feigl, K., & Rabaute, T. (1993). The displacement field of the Landers earthquake mapped by radar interferometry. *Nature*, *364*, 138−142.

Newman, A. V., Dixon, T. H., & Gourmelen, N. (2006). A four-dimensional viscoelastic deformation model for Long Valley Caldera, California, between 1995 and 2000. *Journal of Volcanology and Geothermal Research*, *150*(1–3), 244−269.

Peltzer, G., & Rosen, P. A. (1995). Surface displacement of the 17 May 1993 Eureka Valley, California, earthquake observed by SAR interferometry. *Science*, *268*, 1333−1336.

Rosen, P. A., Hensley, S., Gurrola, E., Rogez, F., Chan, S., & Martin, J. (2001). SRTM C-band topographic data quality assessment and calibration activities. *IGARSS'01 Proceedings, July 2001, Sydney, Australia* (pp. 739−741).

Rosen, P. A., Hensley, S., Joughin, I. R., Li, F. K., Madsen, S. N., Rodriguez, E., & Goldstein, R. (2000). Synthetic aperture radar interferometry. *IEEE Proceedings*, *88*, 333−376.

Sorey, M. L., Mc Connell, V. S., & Roeloffs, E. (2003). Summary of recent research in Long Valley caldera, California. *Journal of Volcanology and Geothermal Research*, *127*(3–4), 165−173.

Stanton, J. M. (2001). Galton, Pearson, and the Peas: a brief history of linear regression for statistics instructors. *Journal of Statistics Education*, *9*(3).

Stine, S. W. (1984). Late Holocene lake level fluctuations and island volcanism at Mono Lake, California. *Geological guide to Aspen Valley, Mono Lake, Mono Craters, and Inyo Craters* (pp. 21−49). Palo Alto, CA Genny Smith Books.

Thatcher, W., & Massonnet, D. (1997). Crustal deformation at Long Valley Caldera, eastern California, 1992–1996, inferred from satellite radar interferometry. *Geophysical Research Letters*, *20*, 2519−2522.

USGS, http://quake.wr.usgs.gov/research/deformation/gps/auto/LongValley

Werner, C., Wegmuller, U., Strozzi, T., & Wiesmann, A. (2003). Interferometric point target analysis for deformation mapping. *IGARSS '03 Proceedings, 7, July 2003, Toulouse, France* (pp. 4362−4364).

Xu, W., & Cumming, I. (1999). A region-growing algorithm for InSAR phase unwrapping. *IEEE Transaction on Geoscience and Remote Sensing*, *37*(1), 124−134.

Zebker, H. A., & Villasenor, J. (1992). Decorrelation in interferometric radar echoes. *IEEE Transactions on Geoscience and Remote Sensing*, *30*, 950−959.